

# Supersolid Phases in Ultracold Gases of Microwave Shielded Polar Molecules

Wei Zhang,<sup>1,2,\*</sup> Hongye Liu,<sup>1,2,\*</sup> Fulin Deng,<sup>1</sup> Kun Chen,<sup>1,2,†</sup> Su Yi,<sup>3,‡</sup> and Tao Shi<sup>1,2,§</sup>

<sup>1</sup>*Institute of Theoretical Physics, Chinese Academy of Sciences, Beijing 100190, China*

<sup>2</sup>*School of Physical Sciences, University of Chinese Academy of Sciences, Beijing 100049, China*

<sup>3</sup>*Institute of Fundamental Physics and Quantum Technology & School of Physics Science and Technology, Ningbo University, Ningbo, 315211, China*

(Dated: July 1, 2025)

We propose a novel scheme to realize the supersolid phase in ultracold gases of microwave-shielded polar molecules by engineering an additional anisotropy in inter-molecular dipolar interaction via an elliptically polarized microwave. It is shown through quantum Monte-Carlo calculations that the interplay of the anisotropies between the interaction and trapping potential gives rise to rich quantum phases. Particularly, it is found that the supersolid phase emerges in the parameter regime accessible to current experiments. Our study paves the way for exploring the properties of supersolid phases in ultracold gases of polar molecules.

*Introduction.*—Recent realization of ultracold gases of microwave-shielded polar molecules (MSPMs) [1–5] provides a powerful new platform for exploring correlated many-body phases with unprecedented control. On the one hand, the realization of degenerate NaK molecular gases [1–3] and, subsequently, the ultracold tetramers [3] open up a new path toward the creation of the long-sought  $p$ -wave superfluid. On the other hand, the realization of NaCs condensate [5] bridges the gap between weakly interacting atomic gases and strongly interacting helium-4 [6–8], which paves the way for realizing the elusive supersolid (SS) phase [9–12] beyond the helium paradigm [13, 14].

Supersolidity—marked by the coexistence of crystalline order and superfluidity—has attracted extensive interest in ultracold atomic systems, including spin-orbit-coupled Bose-Einstein condensates [15], atoms in optical cavities [16], and magnetic dipolar gases [17–20]. Fundamentally different from atoms, MSPMs exhibit a competition between long-range dipole-dipole interactions (DDI) and a strong short-range repulsive core due to shielding. This leads to antibunched density-density correlations and a significantly reduced condensate fraction [6, 8], placing the system beyond the scope of the Gross-Pitaevskii equation and its Lee-Huang-Yang corrections [7]. Although one might expect that increasing interaction strength and density could drive the system into a SS phase, two key limitations arise: i) Experimentally, enhancing DDI [5, 21, 22] inevitably reduces the shielding effect, leading to substantial three-body losses [4]. ii) Theoretically, a strong attractive DDI induces short interparticle distances, where the repulsive shielding potential suppresses long-range phase coherence, drastically reducing the condensate fraction [6, 8]. A striking example is the emergence of a monolayer crystal under strong DDI with single-microwave shielding, where the superfluid fraction vanishes [23]. Therefore, an experimentally feasible scheme for the SS phase should ensure that molecular gases remain at relatively low density.

In this Letter, we propose a scheme to realize the SS phase in ultracold gases of polar molecules shielded by dual microwaves. To this end, we first show that, by replacing the  $\sigma$ -polarized microwave with an elliptically polarized one, the inter-molecular dipolar interaction breaks its cylindrical symmetry around the  $z$  axis. We derive the analytic expression for the effective interaction potential, in which the ellipticity of the microwave acts as a control knob for tuning the anisotropy of the dipolar interaction in the  $xy$  plane. We then investigate the quantum phases of the trapped NaCs gases using the unbiased path-integral Monte Carlo (PIMC) simulations combined with the worm algorithm (WA) [24–31]. On the parameter plane formed by the ellipticity and trap geometry, we map out the finite-temperature phase diagram which consists of the expanding gases (EG), SS, and self-bound droplet (SBD) phases. In particular, the SS phase appears in the parameter regime accessible to the current experiment. More importantly, because the emergence of the SS phase in our scheme takes full advantage of anisotropy of the dipolar interaction, the density of gas required for density modulation is much lower than that without ellipticity, which leads to a significantly extended lifetime of molecular gases.

*Effective inter-molecular interaction.*—Before exploring the many-body properties, let us first determine the effective potential between two molecules shielded by a  $\pi$ -polarized and an elliptically polarized (with ellipticity  $\xi$ ) microwaves. In this configuration, the amplitudes of the  $\sigma^+$ - and  $\sigma^-$ -polarized microwave fields are proportional to,  $\cos\xi$  and  $\sin\xi$ , respectively. Then for  $|\xi| \lesssim 15^\circ$ , the effective potential, up to the second-order perturbation, takes the form [32]

$$V_{\text{eff}}(\mathbf{r}) = \frac{1}{r^3} [C_{3,0}(3\cos^2\theta - 1) + C_{3,2}\sin^2\theta\cos 2\varphi] + \frac{1}{r^6} \sum_{m,m'=-2}^2 C_{6,mm'} Y_{2m}^*(\hat{\mathbf{r}}) Y_{2m'}(\hat{\mathbf{r}}), \quad (1)$$

where  $\theta$  and  $\varphi$  are, respectively, the polar and azimuthal angles of  $\mathbf{r}$ . As can be seen, the  $1/r^3$  dipolar interac-

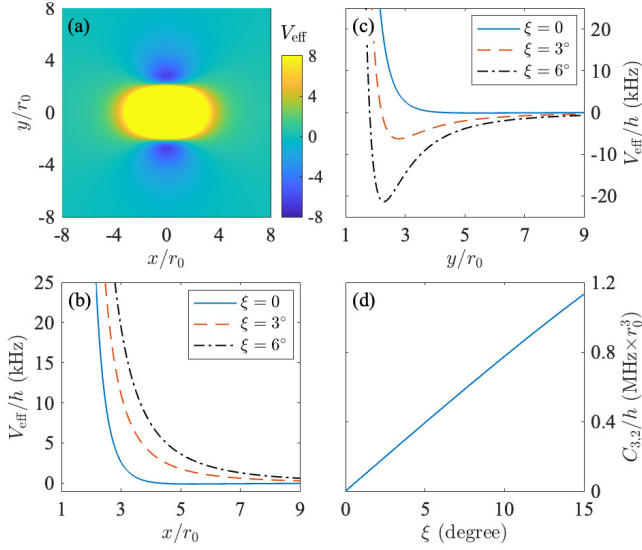


FIG. 1. (a) Effective potential (in units of kHz) on the  $xy$  plane for  $\xi = 3^\circ$ . (b) and (c) show the effective potentials along the  $x$  and  $y$  axes, respectively, for various values of  $\xi$ . (d)  $C_{3,2}$  as a function of  $\xi$ .

tion consists of an isotropic and an anisotropic (on the  $xy$  plane) parts, characterized by  $C_{3,0}$  and  $C_{3,2}$ , respectively. Moreover, the  $1/r^6$  shielding potential is governed by a  $5 \times 5$  symmetric matrix  $C_6$  for interaction strengths. The parity symmetry of the potential further requires  $C_{6,mm} = C_{6,-m,-m}$  and  $C_{6,mm'} = 0$  for  $|m - m'| \neq 0, 2, 4$ . Consequently, the shielding potential is completely determined by six independent parameters, say  $C_{6,00}$ ,  $C_{6,11}$ ,  $C_{6,1-1}$ ,  $C_{6,22}$ ,  $C_{6,20}$ , and  $C_{6,2-2}$ . As shown in the Supplemental Material (SM) [32], all interaction parameters are completely determined by the permanent dipole moment  $d$  of the molecules, the ellipticity  $\xi$ , along with Rabi frequencies ( $\Omega_\sigma, \Omega_\pi$ ) and detunings ( $\delta_\sigma, \delta_\pi$ ) of the  $\sigma$ - and  $\pi$ -polarized microwave fields. Moreover, it can be verified that  $V_{\text{eff}}$  regains its cylindrical symmetry when  $\xi = 0$ . The validity of these analytic results can be justified by directly comparing them with the adiabatic potential [32]. In general,  $C_3$ 's are exact since they describe the long-range interaction; the second-order perturbation results for  $C_6$ 's are fairly accurate, as shown in SM. Nevertheless, the values of  $C_6$ 's can be improved by numerically fitting Eq. (SM2) with the adiabatic potential. Further justification of the effective potential can be performed by comparing the scattering properties calculated using the effective potential with those by multi-channel calculations [32].

To visualize the effective potential, we consider, as a concrete example, the NaCs molecules with a dipole moment  $d = 4.6$  Debye. Following the experimental setup in Ref. [5], the microwave parameters are chosen as  $\Omega_\sigma = 2\pi \times 7.9$  MHz,  $\delta_\sigma = -2\pi \times 8$  MHz, and  $\delta_\pi = -2\pi \times 10$  MHz. In addition, we assume that  $\Omega_\pi = 2\pi \times 6.5$  MHz, which

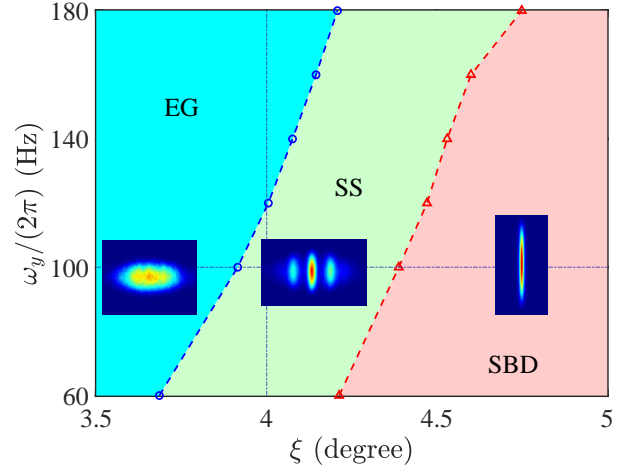


FIG. 2. Phase diagram in the  $\xi$ - $\omega_y$  plane. Insets are the representative column densities  $\bar{n}(x, y)$  in different phases.

leads to  $C_{3,0} \approx 0$ . As a result, the  $1/r^3$  dipolar interaction is solely contributed by the anisotropic part  $C_{3,2}$ . In Fig. 1(a), we map out the typical effective potential in the  $xy$  plane with  $\xi = 3^\circ$ . The long-range behavior of the potential can be understood by noting that  $C_{3,2}$  is proportional to  $\sin 2\xi$  [32] and its sign is uniquely determined by  $\xi$ . Consequently, the dipolar interaction is repulsive (attractive) along the  $x$  ( $y$ ) axis. In addition, the long-range dipolar interaction along the  $z$  direction nearly vanishes. As to the shielding potential, the size of the shielding potential is over  $r_0$  ( $\equiv 10^3 a_0$  with  $a_0$  being the Bohr radii). It remains repulsive along all three dimensions even for nonzero  $\xi$ . Since changing the sign of  $\xi$  only rotates the potential along the  $z$  axis by  $\pi/2$ , we assume, without loss of generality, that  $\xi \geq 0$  throughout this work. To reveal more details about the effective potential, we plot, in Fig. 1(b) and (c), the  $x$  and  $y$  dependence of the potential, respectively, for various  $\xi$ 's. Since the repulsion (attraction) along the  $x$  ( $y$ ) axis is strengthened with  $\xi$ , the planar anisotropy is enhanced by increasing  $\xi$ . This can also be seen in Fig. 1(d) where  $C_{3,2}$  appears as an increasing function of  $\xi$ . Finally, we point out that the effective potential along the  $z$  axis remains roughly unchanged with  $\xi$ .

*Many-body quantum phases.*— To further investigate the many-body quantum phases, we consider a trapped gas of  $N$  NaCs molecules at temperature  $T$ . In second-quantized form, the total Hamiltonian of the system reads

$$H = \int d\mathbf{r} \left[ \frac{\hbar^2}{2M} \nabla \hat{\psi}^\dagger(\mathbf{r}) \nabla \hat{\psi}(\mathbf{r}) + U(\mathbf{r}) \hat{\psi}^\dagger(\mathbf{r}) \hat{\psi}(\mathbf{r}) \right] + \frac{1}{2} \int d\mathbf{r} d\mathbf{r}' V_{\text{eff}}(\mathbf{r} - \mathbf{r}') \hat{\psi}^\dagger(\mathbf{r}) \hat{\psi}^\dagger(\mathbf{r}') \hat{\psi}(\mathbf{r}') \hat{\psi}(\mathbf{r}), \quad (2)$$

where  $M$  is the molecular mass,  $\hat{\psi}(\mathbf{r})$  is the field oper-

ator, and  $U(\mathbf{r}) = M(\omega_x^2 x^2 + \omega_y^2 y^2 + \omega_z^2 z^2)/2$  is the external trap with  $\omega_{i=x,y,z}$  being the trap frequencies. To be specific, we fix the temperature at  $T = 4$  nK and the trap frequencies at  $\omega_x = 2\pi \times 20$  Hz and  $\omega_z = 2\pi \times 80$  Hz. This reduces the system's free parameters to  $\xi$  and  $\omega_y$ . We explore the finite-temperature many-body phases employing the PIMC based on WA [24–26], which provides an unbiased and numerically exact framework for investigating the thermodynamic properties of the system under realistic experimental conditions, circumventing the need for mean-field approximations or uncontrolled expansions.

Figure 2 summarizes the phase diagram on the  $\xi$ - $\omega_y$  parameter plane where three distinct phases exist. The insets are representative column densities  $\bar{n}(x, y) = \int dz n(\mathbf{r})$  for different phases. In the EG phase, the cloud is featured by a single density peak that eventually expands and disappears if  $\omega_x = 0$ . The typical condensate fraction  $f_c$  is over 0.7, here  $f_c \equiv N_0/N$  with  $N_0$  being the largest eigenvalue of the first-order correlation function  $G^{(1)}(\mathbf{r}, \mathbf{r}') \equiv \langle \hat{\psi}^\dagger(\mathbf{r}) \hat{\psi}(\mathbf{r}') \rangle$ . The transition from EG to SS phase is determined by the criterion  $S(k_{\text{sub}}, 0, 0) > 1\%$ , where  $S(\mathbf{k}) = |\int d\mathbf{r} n(\mathbf{r}) e^{-i\mathbf{k}\cdot\mathbf{r}} / N|^2$  is the structure factor, and  $k_{\text{sub}} \neq 0$  is the momentum at the sub-dominated peak along the  $x$ -direction [cf. second rows of Figs. 3 and 4]. In the SS phase, the gas density along the  $x$  axis is modulated such that the whole gas possesses multiple density peaks. Meanwhile, the system remains fully coherent, which gives rise to superfluidity. We remark that since in the presence of density modulation it is challenging to diagonalize  $G^{(1)}(\mathbf{r}, \mathbf{r}')$  with sufficient precision, we measure the peak-to-peak coherence using the reduced normalized correlation function:

$$g_{\text{pp}}^{(1)} \equiv \frac{\bar{G}^{(1)}(x_p, x'_p)}{\sqrt{\bar{G}^{(1)}(x_p, x_p) \bar{G}^{(1)}(x'_p, x'_p)}} \quad (3)$$

where  $\bar{G}^{(1)}(x, x') = \int dy dz dy' dz' G^{(1)}(\mathbf{r}, \mathbf{r}')$ ,  $x_p$  and  $x'_p$  are the  $x$  coordinates of the dominant central peak and its neighboring peak, respectively. In Fig. 2, we adopt the criterion  $g_{\text{pp}}^{(1)} \leq 1\%$  for the transition from SS to the SBD phase. Finally, in the SBD phase, the peak-to-peak coherence vanishes such that different density peaks become fully separated. Moreover, the dominant central droplet is self-bound in the absence of the  $x$ -direction trap. We note that away from the SS-SBD boundary, the side peaks may disappear completely such that the whole system becomes a single droplet.

*Transitions induced by ellipticity.*—To reveal more details about the quantum phases, we explore the transitions induced by varying ellipticity with the  $y$ -direction trap frequency being fixed at  $\omega_y = 2\pi \times 100$  Hz. In Fig. 3, we plot the column density  $\bar{n}(x, y)$  (first row) and the structure factor  $S(k_x, 0, 0)$  (second row) for the representative values of  $\xi$  [from (a) to (e)].

At  $\xi = 0^\circ$ , the system forms a single gas cloud elongated along the  $x$  direction, consistent with the trap geometry. Consequently,  $S(k_x, 0, 0)$  is a single narrow peak in the momentum space. As  $\xi$  increases, the attraction along the  $y$  direction becomes stronger, which, analogous to conventional dipolar gases, can lead to a roton instability and trigger density modulation. To see this, we model the effective interaction using the pseudopotential

$$V_{\text{pp}}(\mathbf{r}) = g_s \delta(\mathbf{r}) + \frac{C_{3,2}}{r^3} \sin^2 \theta \cos 2\varphi, \quad (4)$$

where  $g_s = 4\pi\hbar^2 a_s / M$  with  $a_s$  being the  $s$ -wave scattering length computed using the full effective potential Eq. (SM2). Then, for a homogeneous condensate of the density  $n$ , the dispersion relation for the Bogoliubov excitation is

$$\epsilon(\mathbf{k}) = \sqrt{\epsilon_k^0 [\epsilon_k^0 + 2g_s n (1 - \varepsilon_{3,2} \sin^2 \theta_k \cos 2\varphi_k)]}, \quad (5)$$

where  $\epsilon_k^0 = \hbar^2 k^2 / (2M)$ ,  $\varepsilon_{3,2} = MC_{3,2} / (3\hbar^2 a_s)$ , and  $\theta_k$  and  $\varphi_k$  are the polar and azimuthal angles of  $\mathbf{k}$ , respectively. Apparently, for our system with  $\varepsilon_{3,2} > 0$ , the instability can be most easily induced along the direction  $(\theta_k, \varphi_k) = (\pi/2, 0)$ , i.e., the  $x$  axis. Although this instability may seem independent of  $k$  from Eq. (5), it actually sets in at a finite  $k_x$  for trapped gases. Indeed, as shown in Fig. 3(b1) and (b2), our numerical simulations indicate that the density becomes modulated along the  $x$  axis at  $\xi \approx 3.9^\circ$ . Here, because different density peaks are not well-separated, one can barely see any additional peaks on  $S(k_x, 0, 0)$  other than the one at  $k_x = 0$ . We note that the peak density ( $\sim 1.5 \times 10^{12} \text{ cm}^{-3}$ ) of the gas in Fig. 3(b1) is at the same order of magnitude as that of NaCs condensate realized in experiment [33] and is much lower than that of the SS state in Dy atomic gas ( $5 \times 10^{14} \text{ cm}^{-3}$  in [18]).

Independent of phase coherence, the density modulation can be alternatively understood from the long-range repulsive interaction along the  $x$  direction. Roughly speaking, when the center of the trap is occupied, it is energetically favorable for its immediate neighbors along the  $x$  axis to be less occupied, while more distant regions become more populated. Moreover, the attractive interaction along the  $y$  axis also facilitates the formation of the density modulation, since all density peaks now have a shape more stretched along the  $y$  axis, which further lowers the interaction energy. Finally, the weak  $x$ -direction confinement further assists the formation of the crystalline order by permitting gas expansion along the axis with minimal potential energy cost. Therefore, the appearance of the SS phase at a relatively low density is due to the interplay between the anisotropies of the interaction and the confinement.

Now, for  $\xi = 4.0^\circ$  [Fig. 3(c1) and (c2)], well-separated density peaks form. Consequently, the structure factor is characterized by two side peaks at  $k_x r_0 = \pm 0.0847(6)$ ,

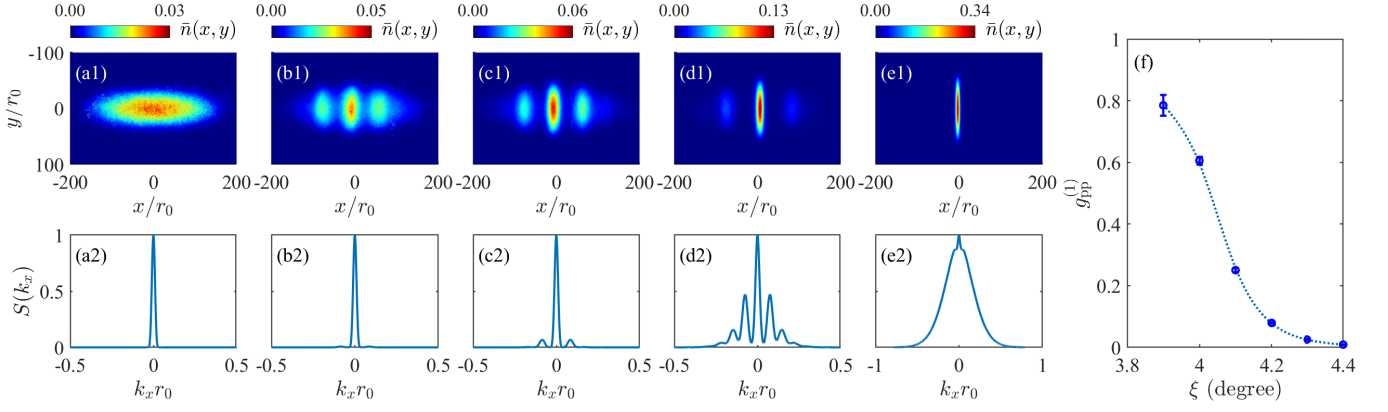


FIG. 3. Column densities (first row) and structure factors (second row) for  $\xi = 0^\circ$  (a),  $3.9^\circ$  (b),  $4.0^\circ$  (c),  $4.2^\circ$  (d), and  $4.6^\circ$  (e). (f) shows the peak-to-peak coherence versus  $\xi$  in the SS phase. Here, column densities are plotted using  $10^6 \sim 10^7$  snapshots in the Markov chain generated from a single random seed, while structure factors and the peak-to-peak coherence are averaged over 40-64 random seeds.

a signature of the density modulation. When  $\xi$  is further increased to  $4.2^\circ$ , as shown in Fig. 3(d1), the central peak becomes more stretched along the  $y$  axis and accumulates more molecules with a dramatically increased peak density. Such configuration yields a much lower interaction energy. In the momentum space, as shown in Fig. 3(d2), more side peaks emerge in  $S(k_x, 0, 0)$ . Particularly, the subdominant peaks shift to  $k_x r_0 = \pm 0.0758(7)$ . To confirm the superfluidity in the presence of density modulation, we plot, in Fig. 3(f), the  $\xi$  dependence of the peak-to-peak coherence  $g_{pp}^{(1)}$ . As can be seen, the coherence monotonically decreases with  $\xi$  and becomes negligibly small at  $\xi = 4.4^\circ$ , marking the boundary of the SS phase. We point out that the superfluidity of the gas can also be confirmed by examining the superfluid fraction  $f_{sf}^{(i)}$  evaluated in PIMC-WA through the system's response to an imposed rotation around the  $i$ th axis. The results are presented in SM [32]. Because the system is highly anisotropic,  $f_{sf}^{(i)}$  for different axes are distinct. In addition, since none of  $f_{sf}^{(i)}$  exactly measure the superfluidity along the  $x$  axis, they remain finite even when the coherence vanishes.

Finally, in the droplet phase with  $\xi = 4.6^\circ$ , as shown in Fig. 3(e1), all side peaks merge into the central one such that it becomes a filament with a peak density ten times larger than that of the  $\xi = 0^\circ$  case. Correspondingly,  $S(k_x, 0, 0)$  exhibits a broadened peak [Fig. 3(e2)], indicating the loss of the crystalline order.

*Transitions induced by confinement.*—We now turn to explore the phase transitions induced by varying  $\omega_y$ . For this purpose, we fix the ellipticity at  $\xi = 4^\circ$  and allow  $\omega_y/(2\pi)$  to vary between 20 to 180 Hz. Figure 4 plots the typical column densities  $\bar{n}(x, y)$  (first row) and structure factors  $S(k_x, 0, 0)$  (second row) for different values of  $\omega_y$ .

For  $\omega_y/(2\pi) = 20$  Hz, the trapping potential is isotropic in the  $xy$  plane and is more tightly confined along the  $z$

axis. However, due to the anisotropy of the interaction, the gas, as shown in Fig. 4(a1), is dramatically stretched along the  $y$  axis. Accordingly,  $S(k_x, 0, 0)$  exhibits a single broad peak in momentum space [see Fig. 4(a2)]. Moreover, since the system is self-bound, it belongs to the SBD phase. The condensate fraction is  $f_c = 0.63(1)$ .

Following the increase of  $\omega_y$ , the confining potential squeezes the gas in the  $y$  direction. To keep the interaction energy low, the gas roughly maintains its shape and shrinks as a whole. In consequence, the peak density of the gas increases significantly. As the inter-molecular spacing becomes comparable to the size of the shielding potential, further increase of the peak density becomes infeasible. Instead, the gas starts to spread along the  $x$  axis which has the weakest confinement. When the gas expands sufficiently along the repulsive  $x$  direction, side density peaks develop to lower the interaction energy, which leads to the crystalline order.

Figure 4(b), (c), and (d) show the column density and the structure factor in the SS phase for  $\omega_y/(2\pi) = 60, 80$ , and  $100$  Hz, respectively. The crystalline order is clearly manifested in the structure factor, where the subdominant peaks shift from  $k_x r_0 = \pm 0.0652(7)$  to  $\pm 0.0764(3)$  and then to  $\pm 0.0847(6)$  as  $\omega_y$  increases. In addition, the central peak is continuously squeezed, accompanied by the growth of the side peaks. Consequently, the crystalline order becomes well formed in Fig. 4(c). When more molecules are squeezed into the side peaks [see Fig. 4(d)], the boundary between the central and side peaks is blurred and the crystalline order is suppressed. In other words, the supersolid starts to melt. In Fig. 4(f), we plot  $g_{pp}^{(1)}$  as a function of  $\omega_y$ . As can be seen, the peak-to-peak coherence monotonically increases with  $\omega_y$ , which is understandable since the peak density of the gas decreases. Finally, as  $\omega_y/(2\pi)$  increases to 180 Hz, the system enters the EG phase for which, as shown in

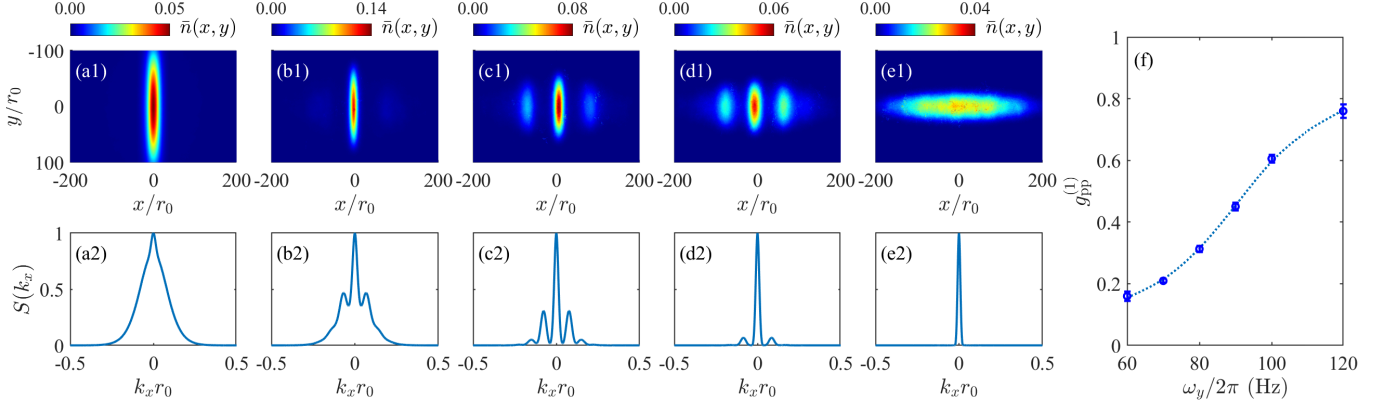


FIG. 4. Column densities (first row) and structure factors (second row) for  $\omega_y/(2\pi) = 20$  (a), 60 (b), 80 (c), 100 (d), and 180 Hz (e). (f) shows the peak-to-peak coherence versus  $\omega_y$  in the SS phase.

Fig. 4(e), the side peaks disappear completely.

**Conclusion.**—For ultracold gases of polar molecules shielded by dual microwaves, we derive an effective potential that is anisotropic on the  $xy$  plane by introducing ellipticity. We demonstrate that by tuning the microwave ellipticity, the SS phase can be realized in ultracold gases of NaCs molecules. We map out the phase diagram on the  $\xi$ - $\omega_y$  plane which shows that the SS phase lies in the parameter regime accessible to current experiments. We have analyzed the underlying physics for the emergence of the density modulation, which shows that through the interplay between anisotropies of interaction and confinement the SS phase can be realized in a gas with relatively low density.

This work was supported by National Key Research and Development Program of China (Grant No. 2021YFA0718304), by the NSFC (Grants No. 12135018, No. 12047503, No. 12474245, and No. 12274331), and by CAS Project for Young Scientists in Basic Research (Grant No. YSBR-057).

\* These authors contributed equally to this work.

† chenkun@itp.ac.cn

‡ yisu@nbn.edu.cn

§ tshi@itp.ac.cn

- [1] A. Schindewolf, R. Bause, X.-Y. Chen, M. Duda, T. Karman, I. Bloch, and X.-Y. Luo, Evaporation of microwave-shielded polar molecules to quantum degeneracy, *Nature* **607**, 677 (2022).
- [2] X.-Y. Chen, A. Schindewolf, S. Eppelt, R. Bause, M. Duda, S. Biswas, T. Karman, T. Hilker, I. Bloch, and X.-Y. Luo, Field-linked resonances of polar molecules, *Nature* **614**, 59 (2022).
- [3] X.-Y. Chen, S. Biswas, S. Eppelt, A. Schindewolf, F. Deng, T. Shi, S. Yi, T. A. Hilker, I. Bloch, and X.-Y. Luo, Ultracold field-linked tetratomic molecules, *Nature* **626**, 283 (2024).

- [4] J. Lin, G. Chen, M. Jin, Z. Shi, F. Deng, W. Zhang, G. Quémener, T. Shi, S. Yi, and D. Wang, Microwave shielding of bosonic nrb molecules, *Phys. Rev. X* **13**, 031032 (2023).
- [5] N. Bigagli, W. Yuan, S. Zhang, B. Bulatovic, T. Karman, I. Stevenson, and S. Will, Observation of bose-einstein condensation of dipolar molecules, *Nature* **631**, 289 (2024).
- [6] W.-J. Jin, F. Deng, S. Yi, and T. Shi, Bose-einstein condensates of microwave-shielded polar molecules (2024), arXiv:2406.06412 [cond-mat.quant-gas].
- [7] T. Langen, J. Boronat, J. Sánchez-Baena, R. Bombín, T. Karman, and F. Mazzanti, Dipolar droplets of strongly interacting molecules, *Phys. Rev. Lett.* **134**, 053001 (2025).
- [8] W. Zhang, K. Chen, S. Yi, and T. Shi, Quantum phases for finite-temperature gases of bosonic polar molecules shielded by dual microwaves (2025), arXiv:2503.02644 [cond-mat.quant-gas].
- [9] E. P. Gross, Unified theory of interacting bosons, *Phys. Rev.* **106**, 161 (1957).
- [10] A. F. Andreev and I. M. Lifshitz, Quantum theory of defects in crystals, *Sov. Phys. JETP* **29**, 1107 (1969).
- [11] A. J. Leggett, Can a solid be "superfluid"? , *Phys. Rev. Lett.* **25**, 1543 (1970).
- [12] G. V. Chester, Speculations on bose-einstein condensation and quantum crystals, *Phys. Rev. A* **2**, 256 (1970).
- [13] M. Boninsegni and N. V. Prokof'ev, Colloquium: Supersolids: What and where are they?, *Rev. Mod. Phys.* **84**, 759 (2012).
- [14] D. Y. Kim and M. H. W. Chan, Absence of supersolidity in solid helium in porous vycor glass, *Phys. Rev. Lett.* **109**, 155301 (2012).
- [15] J.-R. Li, J. Lee, W. Huang, S. Burchesky, B. Shteynas, F. C. Top, A. O. Jamison, and W. Ketterle, A stripe phase with supersolid properties in spin-orbit-coupled bose-einstein condensates, *Nature* **543**, 91 (2017).
- [16] J. Léonard, A. Morales, P. Zupancic, T. Donner, and T. Esslinger, Monitoring and manipulating higgs and goldstone modes in a supersolid quantum gas, *Science* **358**, 1415 (2017), <https://www.science.org/doi/pdf/10.1126/science.aan2608>.
- [17] M. Guo, F. Boettcher, J. Hertkorn, J.-N. Schmidt,

- M. Wenzel, H. P. Buechler, T. Langen, and T. Pfau, The low-energy goldstone mode in a trapped dipolar supersolid, *Nature* **574**, 386 (2019).
- [18] L. Tanzi, E. Lucioni, F. Famà, J. Catani, A. Fioretti, C. Gabbanini, R. N. Bisset, L. Santos, and G. Modugno, Observation of a dipolar quantum gas with metastable supersolid properties, *Phys. Rev. Lett.* **122**, 130405 (2019).
- [19] F. Böttcher, J.-N. Schmidt, M. Wenzel, J. Hertkorn, M. Guo, T. Langen, and T. Pfau, Transient supersolid properties in an array of dipolar quantum droplets, *Phys. Rev. X* **9**, 011051 (2019).
- [20] L. Chomaz, D. Petter, P. Ilzhöfer, G. Natale, A. Trautmann, C. Politi, G. Durastante, R. M. W. van Bijnen, A. Patscheider, M. Sohmen, M. J. Mark, and F. Ferlaino, Long-lived and transient supersolid behaviors in dipolar quantum gases, *Phys. Rev. X* **9**, 021012 (2019).
- [21] F. Deng, X. Hu, W.-J. Jin, S. Yi, and T. Shi, Two- and many-body physics of ultracold molecules dressed by dual microwave fields (2025), arXiv:2501.05210 [cond-mat.quant-gas].
- [22] T. Karman, N. Bigagli, W. Yuan, S. Zhang, I. Stevenson, and S. Will, Double microwave shielding (2025), arXiv:2501.08095 [cond-mat.quant-gas].
- [23] M. Ciardi, K. R. Pedersen, T. Langen, and T. Pohl, Self-bound monolayer crystals of ultracold polar molecules (2025), arXiv:2504.02682 [cond-mat.quant-gas].
- [24] N. Prokof'ev, B. Svistunov, and I. Tupitsyn, Exact, complete, and universal continuous-time worldline monte carlo approach to the statistics of discrete quantum systems, *Journal of Experimental and Theoretical Physics* **87**, 310 (1998).
- [25] M. Boninsegni, N. Prokof'ev, and B. Svistunov, Worm algorithm for continuous-space path integral monte carlo simulations, *Phys. Rev. Lett.* **96**, 070601 (2006).
- [26] M. Boninsegni, N. V. Prokof'ev, and B. V. Svistunov, Worm algorithm and diagrammatic monte carlo: A new approach to continuous-space path integral monte carlo simulations, *Phys. Rev. E* **74**, 036701 (2006).
- [27] K. Chen, L. Liu, Y. Deng, L. Pollet, and N. Prokof'ev, Universal conductivity in a two-dimensional superfluid-to-insulator quantum critical system, *Phys. Rev. Lett.* **112**, 030402 (2014).
- [28] K. Chen, Y. Huang, Y. Deng, A. B. Kuklov, N. V. Prokof'ev, and B. V. Svistunov, Deconfined criticality flow in the heisenberg model with ring-exchange interactions, *Phys. Rev. Lett.* **110**, 185701 (2013).
- [29] M. Boninsegni, N. Prokof'ev, and B. Svistunov, Super-glass phase of  $^4\text{He}$ , *Phys. Rev. Lett.* **96**, 105301 (2006).
- [30] A. Kuklov, L. Pollet, N. Prokof'ev, and B. Svistunov, Transverse quantum superfluids, *Annual Review of Condensed Matter Physics* <https://doi.org/10.1146/annurev-conmatphys-042924-103908> (2024).
- [31] C. Zhang, B. Capogrosso-Sansone, M. Boninsegni, N. V. Prokof'ev, and B. V. Svistunov, Superconducting transition temperature of the bose one-component plasma, *Phys. Rev. Lett.* **130**, 236001 (2023).
- [32] See Supplemental Material for the time-dependent Hamiltonian for two molecules subjected to both an elliptically polarized and a linearly polarized microwave field, the effective interaction potential between two molecules in the highest dressed state, the justification of the effective potential using multi-channel scattering calculations, and the anisotropic superfluid fractions by changing the ellipticity and trap frequency.
- [33] I. Stevenson, S. Singh, A. Elkamshishy, N. Bigagli, W. Yuan, S. Zhang, C. H. Greene, and S. Will, Three-body recombination of ultracold microwave-shielded polar molecules (2024), arXiv:2407.04901 [cond-mat.quant-gas].
- [34] T. Karman and J. M. Hutson, Microwave shielding of ultracold polar molecules, *Phys. Rev. Lett.* **121**, 163401 (2018).
- [35] F. Deng, X.-Y. Chen, X.-Y. Luo, W. Zhang, S. Yi, and T. Shi, Effective potential and superfluidity of microwave-shielded polar molecules, *Phys. Rev. Lett.* **130**, 183001 (2023).
- [36] F. Deng, X. Chen, X. Luo, W. Zhang, S. Yi, and T. Shi, Formation and dissociation of field-linked tetramers (2024), arXiv:2405.13645 [Quantum Physics].
- [37] Z. Idziaszek and P. S. Julienne, Universal rate constants for reactive collisions of ultracold molecules, *Phys. Rev. Lett.* **104**, 113202 (2010).
- [38] M. Lepers, R. Vexiau, M. Aymar, N. Bouloufa-Maafa, and O. Dulieu, Long-range interactions between polar alkali-metal diatoms in external electric fields, *Phys. Rev. A* **88**, 032709 (2013).
- [39] A. L. Fetter, Rotating trapped bose-einstein condensates, *Rev. Mod. Phys.* **81**, 647 (2009).
- [40] D. M. Ceperley, Path integrals in the theory of condensed helium, *Rev. Mod. Phys.* **67**, 279 (1995).



## Supplemental Materials

This Supplemental Material is structured as follows. In Section SM 1, we present a model for polar molecules subjected to both an elliptically polarized and a linearly polarized microwave field, leading to a time-dependent two-molecule Hamiltonian. In Section SM 2, we employ Floquet theory to derive the effective interaction potential for two molecules in the highest dressed state, which shows excellent agreement with the adiabatic potential. Section SM 3 validates this effective potential through multi-channel scattering calculations. In Section SM 4, we demonstrate the anisotropic superfluid fractions by changing the ellipticity and trap frequency.

### SM 1. SINGLE-MOLECULE EIGENSTATES AND TWO-BODY INTERACTIONS

We consider an ultracold gas of bialkali polar molecules in the  $^1\Sigma(v=0)$  state, which can be treated as rigid rotors. At ultracold temperatures, it is sufficient to focus on the lowest rotational state  $|J, M_J\rangle = |0, 0\rangle$  and the first excited manifold  $|J=1, M_J=0, \pm 1\rangle$ , separated by an energy  $\hbar\omega_e$ . Each molecule possesses a permanent electric dipole moment  $d\hat{\mathbf{d}}$ , oriented along the internuclear axis represented by the unit vector  $\hat{\mathbf{d}}$ . To maintain the shielding effect, we apply an elliptically polarized microwave field with elliptic angle  $\xi$ , along with a  $\pi$ -polarized microwave. As illustrated in Fig. SM1, these fields couple the transitions  $|0, 0\rangle \leftrightarrow |1, \pm 1\rangle$  and  $|0, 0\rangle \leftrightarrow |1, 0\rangle$ , with Rabi-frequencies  $\Omega_\sigma$  and  $\Omega_\pi$ , respectively. The corresponding microwave frequencies  $\omega_\sigma$  and  $\omega_\pi$  are blue detuned from the rotational transition frequency  $\omega_e$ , with detunings  $\delta_{\sigma,\pi} = \omega_e - \omega_{\sigma,\pi}$ .

In the frame co-rotating with microwave fields, the internal-state Hamiltonian for a single molecule is time-independent and takes the form

$$\begin{aligned} \hat{h}_{\text{in}} = & \delta_\sigma (|\xi_+\rangle\langle\xi_+| + |\xi_-\rangle\langle\xi_-|) + \delta_\pi |1, 0\rangle\langle 1, 0| \\ & + \left( \frac{\Omega_\sigma}{2} |\xi_+\rangle\langle 0, 0| + \frac{\Omega_\pi}{2} |1, 0\rangle\langle 0, 0| + \text{H.c.} \right), \end{aligned} \quad (\text{SM1})$$

where  $|\xi_+\rangle = \cos\xi|1, 1\rangle + \sin\xi|1, -1\rangle$ , and  $|\xi_-\rangle = \cos\xi|1, -1\rangle - \sin\xi|1, 1\rangle$  are determined by the elliptic angle of the microwave. In the basis  $\{|0, 0\rangle, |\xi_+\rangle, |1, 0\rangle, |\xi_-\rangle\}$ , the single-molecule Hamiltonian reads

$$\hat{h}_{\text{in}} = \begin{pmatrix} 0 & \frac{\Omega_\sigma}{2} & \frac{\Omega_\pi}{2} & 0 \\ \frac{\Omega_\sigma}{2} & \delta_\sigma & 0 & 0 \\ \frac{\Omega_\pi}{2} & 0 & \delta_\pi & 0 \\ 0 & 0 & 0 & \delta_\sigma \end{pmatrix}, \quad (\text{SM2})$$

The single-molecule Hamiltonian  $\hat{h}_{\text{in}}$  can be analytically diagonalized by an unitary transformation

$$U_1 = \begin{pmatrix} \cos\alpha & 0 & -\sin\alpha\cos\gamma & \sin\alpha\sin\gamma \\ \sin\alpha\cos\beta & 0 & \cos\alpha\cos\beta\cos\gamma - \sin\beta\sin\gamma & -\cos\alpha\cos\beta\sin\gamma - \sin\beta\cos\gamma \\ \sin\alpha\sin\beta & 0 & \cos\alpha\sin\beta\cos\gamma + \cos\beta\sin\gamma & -\cos\alpha\sin\beta\sin\gamma + \cos\beta\cos\gamma \\ 0 & 1 & 0 & 0 \end{pmatrix}, \quad (\text{SM3})$$

which is conveniently parameterized by three Euler angles  $\alpha, \beta$ , and  $\gamma$ . The columns of  $U_1$  are the eigenvectors of  $\hat{h}_{\text{in}}$  which, from left to right, are denoted as  $|+\rangle$ ,  $|\xi_-\rangle$ ,  $|-\rangle$ , and  $|0\rangle$ . The corresponding eigenenergies are denoted as  $E_+$ ,  $\delta_\sigma$ ,  $E_-$ , and  $E_0$ , respectively. We note that in the limit  $\Omega_\pi \rightarrow 0$  the eigenstates and eigenenergies can be expressed explicitly as  $|+\rangle \rightarrow \cos\alpha|0, 0\rangle + \sin\alpha|\xi_+\rangle$ ,  $|-\rangle \rightarrow \sin\alpha|0, 0\rangle - \cos\alpha|\xi_+\rangle$ ,  $|0\rangle \rightarrow |1, 0\rangle$ ,  $E_\pm \rightarrow (\delta_\sigma \pm \Omega_{\text{eff}})/2$ , and  $E_0 \rightarrow \delta_\pi$ , where  $\Omega_{\text{eff}} = \sqrt{\delta_\sigma^2 + \Omega_\sigma^2}$  and the Euler angles are known analytically, i.e.,  $(\alpha, \beta, \gamma) = (\arccos[(1 - \delta_\sigma/\Omega_{\text{eff}})/2], 0, 0)$ . The energy level structure in the single-molecule subspace is shown in Fig. SM1a.

Now, for two molecules with dipole moments  $d\hat{\mathbf{d}}_1$  and  $d\hat{\mathbf{d}}_2$ , the inter-molecular DDI is

$$\begin{aligned} V_{\text{dd}}(\mathbf{r}) &= \frac{d^2}{4\pi\epsilon_0 r^3} [\hat{\mathbf{d}}_1 \cdot \hat{\mathbf{d}}_2 - 3(\hat{\mathbf{d}}_1 \cdot \hat{\mathbf{r}})(\hat{\mathbf{d}}_2 \cdot \hat{\mathbf{r}})] \\ &= -\frac{\eta}{r^3} \sum_{m=-2}^2 Y_{2m}^*(\hat{\mathbf{r}}) \Sigma_{2,m}, \end{aligned} \quad (\text{SM4})$$

where  $\eta = \sqrt{8\pi/15} d^2/\epsilon_0$  with  $\epsilon_0$  being the electric permittivity of vacuum,  $r = |\mathbf{r}|$ ,  $Y_{2m}(\hat{\mathbf{r}})$  are spherical harmonics, and  $\Sigma_{2,m}$  are components of the rank-2 spherical tensor defined as  $\Sigma_{2,0} = (\hat{d}_1^+ \hat{d}_2^- + \hat{d}_1^- \hat{d}_2^+ + 2\hat{d}_1^0 \hat{d}_2^0)/\sqrt{6}$ ,  $\Sigma_{2,\pm 1} = (\hat{d}_1^+ \hat{d}_2^0 +$

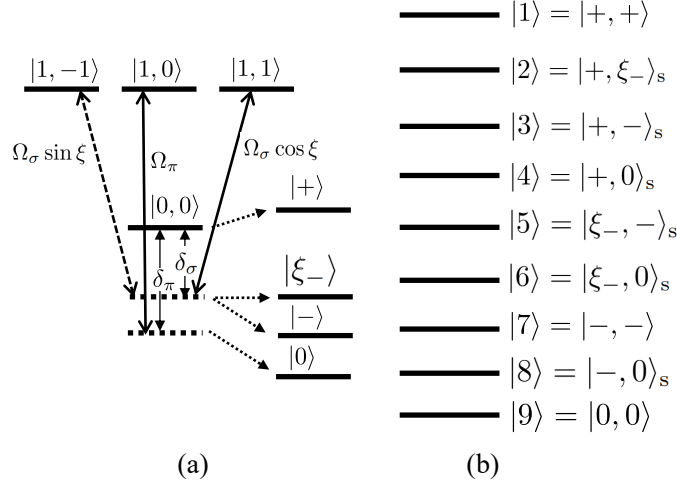


FIG. SM1. Schematics of the dressed-state energy levels. (a) Single-molecule states. (b) Two-molecule states in the symmetric subspace.

$\hat{d}_1^0 \hat{d}_2^\pm / \sqrt{2}$ , and  $\Sigma_{2,\pm 2} = \hat{d}_1^\pm \hat{d}_2^\pm$  with  $\hat{d}_j^\pm = Y_{1,\pm 1}(\hat{\mathbf{d}}_j)$  and  $\hat{d}_j^0 = Y_{1,0}(\hat{\mathbf{d}}_j)$ . In the rotating frame,  $\hat{d}_j^\pm$  and  $\hat{d}_j^0$  become time-dependent. and in the basis  $|J, M_J\rangle$  these operators can be written out explicitly as

$$\begin{aligned}\hat{d}_j^0 &= \frac{1}{\sqrt{4\pi}} (|0, 0\rangle \langle 1, 0| e^{-i\omega_\pi t} + \text{h.c.}), \\ \hat{d}_j^+ &= \frac{1}{\sqrt{4\pi}} (|1, 1\rangle \langle 0, 0| e^{i\omega_\sigma t} - |0, 0\rangle \langle 1, -1| e^{-i\omega_\sigma t}), \\ \hat{d}_j^- &= -(\hat{d}_j^+)^\dagger.\end{aligned}\tag{SM5}$$

After substituting the above spherical components of the vector into  $\Sigma_{2m}$ , we find

$$\begin{aligned}\Sigma_{2,0} &= \frac{1}{4\pi\sqrt{6}} \left( 2|1, 0\rangle \langle 0, 0| \otimes |0, 0\rangle \langle 1, 0| - |1, 1\rangle \langle 0, 0| \otimes |0, 0\rangle \langle 1, 1| - |0, 0\rangle \langle 1, -1| \otimes |1, -1\rangle \langle 0, 0| + \text{h.c.} \right), \\ \Sigma_{2,1} &= \frac{1}{4\pi\sqrt{2}} \left[ (|1, 1\rangle \langle 0, 0| \otimes |0, 0\rangle \langle 1, 0| + |0, 0\rangle \langle 1, 0| \otimes |1, 1\rangle \langle 0, 0|) e^{i\omega t} \right. \\ &\quad \left. - (|0, 0\rangle \langle 1, -1| \otimes |1, 0\rangle \langle 0, 0| + |1, 0\rangle \langle 0, 0| \otimes |0, 0\rangle \langle 1, -1|) e^{-i\omega t} \right], \\ \Sigma_{2,2} &= -\frac{1}{4\pi} (|1, 1\rangle \langle 0, 0| \otimes |0, 0\rangle \langle 1, -1| + |0, 0\rangle \langle 1, -1| \otimes |1, 1\rangle \langle 0, 0|),\end{aligned}$$

where, according to the rotating-wave approximation, we have neglected time-dependent terms with higher frequencies  $\omega_+$  and  $\omega_\pi$  (of the order of GHz) and retained those with the lower frequency  $\omega = \omega_\sigma - \omega_\pi$  (of the order of MHz typically).

To proceed further, the Hamiltonian for the relative motion of two molecules is

$$\hat{H}_2 = -\frac{\hbar^2 \nabla^2}{M} + \sum_{j=1,2} \hat{h}_{\text{in}}(j) + V_{\text{dd}}(\mathbf{r}, t),$$

where  $M$  is the mass of the molecule and  $\hat{h}_{\text{in}}(j)$  denotes the internal-state Hamiltonian of the  $j$ th molecule. And we have explicitly expressed  $V_{\text{dd}}$  as a function of  $t$  in the rotating frame. Since  $\hat{H}_2$  possesses a parity symmetry, the symmetric and antisymmetric two-particle internal states are decoupled in the Hamiltonian  $\hat{H}_2$ . We shall only focus on the ten-dimensional symmetric subspace in which the microwave shielded two-molecule state  $|1\rangle \equiv |+\rangle \otimes |+\rangle$  lies. Further simplification can be made by noting that  $|1\rangle$  only couples to the following eight two-molecule states:  $|2\rangle \equiv |+, \xi_-\rangle_s$ ,  $|3\rangle \equiv |+, -\rangle_s$ ,  $|4\rangle \equiv |+, 0\rangle_s$ ,  $|5\rangle \equiv |\xi_-, -\rangle_s$ ,  $|6\rangle \equiv |\xi_-, 0\rangle_s$ ,  $|7\rangle \equiv |-\rangle \otimes |-\rangle$ ,  $|8\rangle \equiv |-, 0\rangle_s$ , and  $|9\rangle \equiv |0\rangle \otimes |0\rangle$ , where  $|i, j\rangle_s = (|i\rangle \otimes |j\rangle + |j\rangle \otimes |i\rangle) / \sqrt{2}$  represents the symmetrized two-molecule state. The corresponding energies of these two-particle states are denoted as  $E_{\nu=1\sim 9}^{(\infty)}$ . As a result, these nine two-molecule states form a 9-dimensional (9D) symmetric subspace,  $\mathcal{S}_9 \equiv \text{span}\{|\nu\rangle\}_{\nu=1}^9$ . Now, since we focus on system with all molecules being prepared in the



microwave shielded  $|+\rangle$  state, we may project the interaction  $V_{\text{dd}}(\mathbf{r})$  onto the two-molecule subspace  $\mathcal{S}_9$ . The energy level structure in the two-molecule subspace in the limit  $r \rightarrow \infty$  is shown in Fig. SM1b.

In an attempt to eliminate the time dependence of the  $\hat{H}_2$ , we introduce, in  $\mathcal{S}_9$ , an unitary transformation defined by the diagonal matrix

$$U_2(t) = \text{diag}(1, 1, 1, e^{-i\omega t}, 1, e^{-i\omega t}, 1, e^{-i\omega t}, e^{-2i\omega t}). \quad (\text{SM6})$$

A straightforward calculation shows that the Hamiltonian  $\hat{H}_2$  is transformed into

$$\begin{aligned} \hat{\mathcal{H}}(t) &= U_2^\dagger(t) \hat{H}_2 U_2(t) - iU_2^\dagger(t) \partial_t U_2(t) \\ &= -\frac{\hbar^2 \nabla^2}{M} + \mathcal{E}^{(\infty)} + \mathcal{V}(\mathbf{r}, t), \end{aligned} \quad (\text{SM7})$$

where  $\mathcal{E}^{(\infty)}$  is a diagonal matrix with elements being the energies of the asymptotical state  $|\nu\rangle$  with respect to that of the  $|\nu=1\rangle$  state, i.e.,  $\mathcal{E}_{\nu\nu'}^{(\infty)} = (E_\nu^{(\infty)} - 2E_+) \delta_{\nu\nu'}$ . Moreover, the two-body interaction in the basis  $\{|\nu\rangle\}$  is

$$\mathcal{V}(\mathbf{r}, t) = U_2^\dagger(t) V_{\text{dd}}(\mathbf{r}) U_2(t) = \sum_{s=-3}^3 \mathcal{V}_s(\mathbf{r}) e^{is\omega t}$$

which is decomposed into components according to the time dependence  $e^{is\omega t}$ . Particularly, the components satisfy  $\mathcal{V}_{-s}(\mathbf{r}) = \mathcal{V}_s^\dagger(\mathbf{r})$  and

$$\mathcal{V}_0(\mathbf{r}) = -\frac{\eta}{r^3} \left[ Y_{20}(\hat{\mathbf{r}}) \Sigma_{2,0}^{(0)} + Y_{21}^*(\hat{\mathbf{r}}) \Sigma_{2,1}^{(0)} + Y_{21}(\hat{\mathbf{r}}) \Sigma_{2,1}^{(0)\dagger} + Y_{22}^*(\hat{\mathbf{r}}) \Sigma_{2,2}^{(0)} + Y_{22}(\hat{\mathbf{r}}) \Sigma_{2,2}^{(0)\dagger} \right] \quad (\text{SM8a})$$

$$\mathcal{V}_1(\mathbf{r}) = -\frac{\eta}{r^3} \left[ Y_{20}(\hat{\mathbf{r}}) \Sigma_{2,0}^{(1)} + Y_{21}(\hat{\mathbf{r}}) \Sigma_{2,1}^{(-1)\dagger} + Y_{21}^*(\hat{\mathbf{r}}) \Sigma_{2,1}^{(1)} + Y_{22}(\hat{\mathbf{r}}) \Sigma_{2,2}^{(-1)\dagger} + Y_{22}^*(\hat{\mathbf{r}}) \Sigma_{2,2}^{(1)} \right], \quad (\text{SM8b})$$

$$\mathcal{V}_2(\mathbf{r}) = -\frac{\eta}{r^3} \left[ Y_{20}(\hat{\mathbf{r}}) \Sigma_{2,0}^{(2)} + Y_{21}(\hat{\mathbf{r}}) \Sigma_{2,1}^{(-2)\dagger} + Y_{21}^*(\hat{\mathbf{r}}) \Sigma_{2,1}^{(2)} + Y_{22}^*(\hat{\mathbf{r}}) \Sigma_{2,2}^{(2)} + Y_{22}(\hat{\mathbf{r}}) \Sigma_{2,2}^{(-2)\dagger} \right], \quad (\text{SM8c})$$

$$\mathcal{V}_3(\mathbf{r}) = -\frac{\eta}{r^3} \left[ Y_{21}^*(\hat{\mathbf{r}}) \Sigma_{2,1}^{(3)} + Y_{21}(\hat{\mathbf{r}}) \Sigma_{2,1}^{(-3)\dagger} \right], \quad (\text{SM8d})$$

where  $\Sigma_{2,m}^{(s)}$  are matrices originated from  $\Sigma_{2,m} = \sum_s \Sigma_{2,m}^{(s)} e^{is\omega t}$  that is associated with the time dependence  $e^{is\omega t}$ , which satisfy  $\Sigma_{2,-m}^{(s)} = (-1)^m \Sigma_{2,m}^{(-s)\dagger}$ .

## SM 2. FLOQUET THEORY AND EFFECTIVE POTENTIALS

The time periodicity of the Hamiltonian  $\hat{\mathcal{H}}(t)$  suggests that we may tackle the two-molecule physics using the Floquet theory. Specifically, the solution of the Schrödinger equation,

$$i\hbar \frac{\partial |\psi(t)\rangle}{\partial t} = \hat{\mathcal{H}}(t) |\psi(t)\rangle, \quad (\text{SM9})$$

takes the ‘‘Floquet-Fourier’’ form

$$|\psi(t)\rangle = e^{-i\varepsilon t} \sum_{n=-\infty}^{\infty} e^{-in\omega t} |\psi_n\rangle, \quad (\text{SM10})$$

where  $\varepsilon$  is the quasi-energy of the state and  $|\psi_n\rangle$  is the time-independent harmonic component defined on the 9D Hilbert space  $\mathcal{S}_9$ . It follows from Eq. (SM9) that  $|\psi_n\rangle$  satisfy the time-independent eigenvalue equation:

$$\sum_s \mathcal{H}_s |\psi_{n+s}\rangle - n\omega |\psi_n\rangle = \varepsilon |\psi_n\rangle, \quad n = 0, \pm 1, \pm 2, \dots, \quad (\text{SM11})$$

where the Floquet Hamiltonian is

$$\mathcal{H}_s = \begin{cases} -\hbar^2 \nabla^2 / M + \mathcal{E}^{(\infty)} + \mathcal{V}_0(\mathbf{r}), & \text{for } s = 0; \\ \mathcal{V}_s(\mathbf{r}), & \text{for } 0 < |s| \leq 3; \\ 0, & \text{otherwise.} \end{cases} \quad (\text{SM12})$$

Introducing vector  $|\Psi\rangle = (\dots, |\psi_{-1}\rangle, |\psi_0\rangle, |\psi_1\rangle, \dots)^T$  for the Floquet space wavefunction, Eq. (SM11) can be rewritten into a more compact form as

$$\mathbf{H}|\Psi\rangle = \varepsilon|\Psi\rangle,$$

where, in terms of  $9 \times 9$  block matrices, the Floquet Hamiltonian  $\mathbf{H}$  is a heptadiagonal matrix. Thus one may easily visualize the structure of the Schrödinger Eq. (SM11) through  $\mathbf{H}$ .

With Eq. (SM11), the advantage of performing the transformation  $U_2(t)$  is now understandable. Specifically, in the absence of the  $\pi$ -field,  $U_2(t)$  leads to a time-independent  $\mathcal{H}$ , i.e.,  $\mathcal{H}_s = 0$  for all  $s \neq 0$ , indicating that different Floquet sectors are decoupled and the eigenstates can be obtained directly by diagonalizing  $\mathcal{H}_0$ . Then as the  $\pi$ -polarized microwave is gradually turned on to lower the attractive interaction on the  $xy$  plane, the transitions between different Floquet sectors are also switched on. As a result, through transformation  $U_2$ , we ensure that the transitions between different Floquet sectors in the presence of the  $\pi$  microwave are perturbation. Such structure accelerates the convergence in numerical calculations.

Since the microwave-shielded  $|+\rangle$  state has a sufficiently long lifetime in experiments, a molecular gas prepared in the  $|+\rangle$  state represents an important platform for studying the many-body physics. We can derive an time-independent effective potential to describe two-body scatterings in the  $|+\rangle$  state. We note that the internal-state dynamics is much faster than the motion of molecules, which allows us to employ the Born-Oppenheimer (BO) approximation. Then, for a given  $\mathbf{r}$ , we diagonalize, in the Floquet space, the potential matrix  $\mathbf{V}$  (i.e., the Floquet Hamiltonian  $\mathbf{H}$  with kinetic energy being neglected), which gives rise to

$$\mathbf{V}(\mathbf{r})|V_{n,\nu}^{(\text{ad})}(\mathbf{r})\rangle = V_{n,\nu}^{(\text{ad})}(\mathbf{r})|V_{n,\nu}^{(\text{ad})}(\mathbf{r})\rangle, \quad (\text{SM13})$$

where  $|V_{n,\nu}^{(\text{ad})}(\mathbf{r})\rangle$  is the eigenstate and  $V_{n,\nu}^{(\text{ad})}(\mathbf{r})$  is the eigenenergy. Physically,  $|V_{n,\nu}^{(\text{ad})}(\mathbf{r})\rangle$  is the state adiabatically connects to the asymptotical state  $|n, \nu\rangle$ , i.e., the two-molecule state  $|\nu\rangle$  in the  $n$ -th Floquet sector. In particular, we focus on the eigenstate adiabatically connecting to  $|1\rangle = |++\rangle$  with  $n = 0$  as  $r \rightarrow \infty$ . The corresponding eigenenergy  $V_{0,1}^{(\text{ad})}(\mathbf{r})$  is then the effective potential between two microwave-shielded molecules.

Alternatively, we may analytically derive an highly accurate effective potential,  $V_{\text{eff}}(\mathbf{r})$ , through perturbation theory. For this purpose, we note that the first-order correction to the energy of the  $|1\rangle$  state in the sector  $n = 0$  is

$$[\mathcal{V}_0(\mathbf{r})]_{11} = \langle 1 | V_{\text{dd}}(\mathbf{r}) | 1 \rangle = \frac{1}{r^3} [C_{3,0}(3 \cos^2 \theta - 1) + C_{3,2} \sin^2 \theta \cos 2\varphi], \quad (\text{SM14})$$

where

$$\begin{aligned} C_{3,0} &= \sqrt{\frac{15}{2\pi}} \frac{\eta}{48\pi} (3 \cos 2\beta - 1) \cos^2 \alpha \sin^2 \alpha, \\ C_{3,2} &= \sqrt{\frac{15}{2\pi}} \frac{\eta}{8\pi} \sin^2 \alpha \cos^2 \alpha \sin 2\xi \cos^2 \beta. \end{aligned} \quad (\text{SM15})$$

For fixed  $\delta_\sigma$ ,  $\Omega_\sigma$ ,  $\delta_\pi$ , and  $\xi = 0$ , the Euler angle  $\beta$  increases with  $\Omega_\pi$ . As  $\Omega_\pi$  increases to the threshold value  $\Omega_c$ ,  $\beta$  reaches  $\beta_c = \arccos(1/3)/2$ , resulting in a complete cancellation of the effective DDI, i.e.,  $C_{3,0} = 0$ . Below the completely cancellation point, e.g.,  $\Omega_\pi < \Omega_c$ , the elliptic angle  $\xi > 0$  leads to  $C_{3,2} > 0$ , which can be applied to enhance (reduce) the attractive interaction along the  $y$  ( $x$ )-direction.

Next, the second-order correction can be formally expressed as

$$\sum'_{s,\nu} \frac{|\mathcal{V}_s(\mathbf{r})|_{1\nu}|^2}{\mathcal{E}_{11}^{(\infty)} - [\mathcal{E}_{\nu\nu}^{(\infty)} - s\omega]}, \quad (\text{SM16})$$

where the primed sum excludes the term with  $(s, \nu) = (0, 1)$ . By carefully examining the matrix elements of  $\mathcal{V}_s(\mathbf{r})$ , it turns out that, in Eq. (SM16), only a finite number of terms contribute. After collecting all terms contributing to the second-order correction, the effective potential can now be approximated as

$$\begin{aligned} V_{\text{eff}}(\mathbf{r}) &= \frac{1}{r^3} [C_{3,0}(3 \cos^2 \theta - 1) + C_{3,2} \sin^2 \theta \cos 2\varphi] \\ &\quad + \frac{\eta^2}{r^6} \sum_{mm'} C_{6,mm'} Y_{2m}^*(\hat{r}) Y_{2m'}(\hat{r}), \end{aligned} \quad (\text{SM17})$$

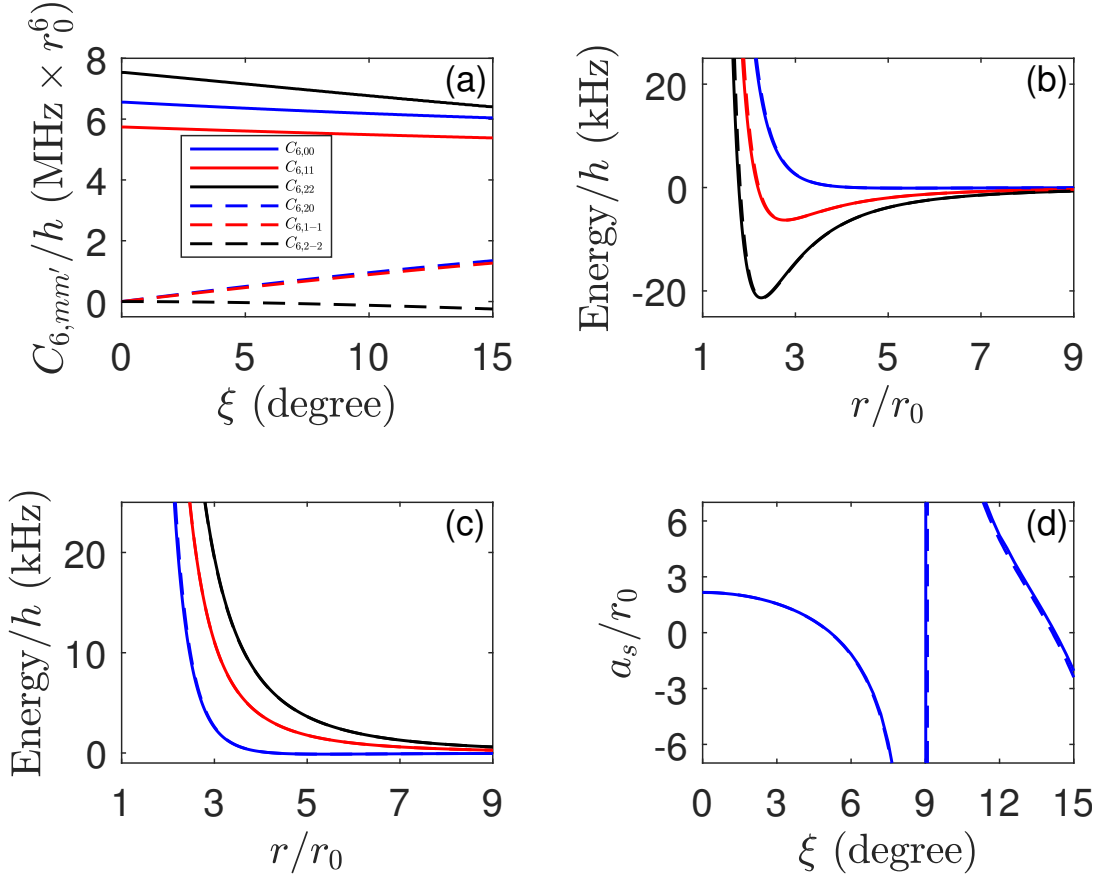


FIG. SM2. (a) Elements of the matrix  $C_6$  as functions of  $\xi$ . (b)-(c): Adiabatic and effective potentials for  $\xi = 0^\circ$  (blue),  $3^\circ$  (red), and  $6^\circ$  (black). Solid curves represent the adiabatic potentials, while dashed curves show the corresponding effective potentials. (b) Potentials along the  $y$ -direction. (c) Potentials along the  $x$ -direction. (d) Excellent agreement between the  $s$ -wave scattering lengths  $a_s$  obtained from the effective potential and from the full coupled-channel calculation. The microwave parameters are:  $\delta_\sigma/(2\pi) = -8$  MHz,  $\Omega_\sigma/(2\pi) = 7.9$  MHz,  $\delta_\pi/(2\pi) = -10$  MHz, and  $\Omega_\pi/(2\pi) = 6.5$  MHz.

where the symmetric matrix  $C_6$  in the basis  $Y_{2,m=2,\dots,-2}(\hat{r})$  can be obtained analytically in terms of the matrix elements  $(\Sigma_{2,m}^{(s)})_{1\nu}$ ,  $\mathcal{E}_{\nu\nu}^{(\infty)}$ , and  $\omega$ . The parity symmetry imposes  $C_{6,mm} = C_{6,-m,-m}$  and non-vanishing  $C_{6,mm'}$  with  $m' = m, m \pm 2, m \pm 4$ , which determines the structure

$$C_6 = \begin{pmatrix} C_{6,22} & 0 & C_{6,20} & 0 & C_{6,2-2} \\ 0 & C_{6,11} & 0 & C_{6,1-1} & 0 \\ C_{6,20} & 0 & C_{6,00} & 0 & C_{6,20} \\ 0 & C_{6,1-1} & 0 & C_{6,11} & 0 \\ C_{6,2-2} & 0 & C_{6,20} & 0 & C_{6,22} \end{pmatrix}. \quad (\text{SM18})$$

In Fig. SM2(a), we show the interaction strengths  $C_{6,mm'}$  as functions of  $\xi$ . In Figs. SM2(b)-(c), we compare the effective potential  $V_{\text{eff}}(\mathbf{r})$  (dashed lines) with the adiabatic potential  $V^{(\text{ad})}(\mathbf{r})$  (solid lines) along the  $y$ - and  $x$ -directions for various values of  $\xi$ . The attractive interaction along the  $x$ -direction is suppressed and along the  $y$ -direction is enhanced for  $\xi > 0$ . The analytical expression in Eq. (SM17) provides a highly accurate form for the molecular interaction, which is crucial for investigating many-body physics.

### SM 3. MULTICHANNEL SCATTERING COMPUTATION IN FLOQUET SPACE

In this Appendix, we turn to formulate the multi-channel scatterings for Floquet-Bloch states. To solve Eq. (SM11), we expand the eigenstate wavefunction  $\psi_{n,\nu}(\mathbf{r}) = \langle \nu | \psi_n(\mathbf{r}) \rangle$  in the partial-wave basis as

$$\psi_{n,\nu}(\mathbf{r}) = \frac{1}{r} \sum_{lm} \phi_{n\nu lm}(r) Y_{lm}(\hat{\mathbf{r}}), \quad (\text{SM19})$$

where  $\phi_{n\nu lm}$  are the radial wavefunctions.

To proceed further, it is convenient to introduce the column vector  $\Phi(\mathbf{r})$  formed by the elements  $\phi_{n\nu lm}(r)$ . The Schrödinger equation for the radial wavefunction can then be written as

$$\partial_r^2 \Phi(r) + \mathbf{W}(r) \Phi(r) = 0, \quad (\text{SM20})$$

where the matrix  $\mathbf{W}$  is defined by the elements

$$W_{n\nu lm, n'\nu' l'm'}(r) = \left[ k_{n\nu}^2 - \frac{l(l+1)}{r^2} \right] \delta_{nn'} \delta_{\nu\nu'} \delta_{ll'} \delta_{mm'} - M \sum_{s=-3}^3 \delta_{n+s, n'} V_{\nu lm, \nu' l'm'}^{(s)}(r) \quad (\text{SM21})$$

with  $k_{n\nu} = \left[ M \left( \varepsilon - \mathcal{E}_{\nu\nu}^{(\infty)} + n\omega \right) \right]^{1/2}$  being the incident momentum with respect to the  $n$ th Floquet sector and the  $\nu$ th dressed channel and

$$V_{\nu lm, \nu' l'm'}^{(s)}(r) = \int d\hat{\mathbf{r}} Y_{lm}^*(\hat{\mathbf{r}}) [\mathcal{V}_s(\mathbf{r})]_{\nu\nu'} Y_{l'm'}(\hat{\mathbf{r}}) \quad (\text{SM22})$$

can be evaluated analytically.

To solve the multi-channel scattering problem, we numerically evolve Eq. (SM20) from a ultraviolet cutoff  $r_{UV}$  to a sufficiently large value  $r_\infty$  using the log-derivative propagator method. Here, we impose a capture boundary condition [S34] at  $r_{UV}$ . It turns out that the choice of  $r_{UV}$  does not affect the result if it is deep inside the shielding core [S21, S35, S36]. We remark that to account for the short-range effects in scatterings, we also include, in numerical calculations, the universal van der Waals interaction through the replacement  $\mathcal{V}_0(\mathbf{r}) \rightarrow \mathcal{V}_0(\mathbf{r}) - C_{\text{vdW}}/r^6$ , where  $C_{\text{vdW}}$  is the strength of the universal van der Waals interaction [S37]. Since  $C_{\text{vdW}}$  is generally much smaller than the microwave shielding strength  $C_6$  [S38], the  $C_{\text{vdW}}$  term only takes effect at short distance.

Then to obtain the scattering matrix, we compare  $\phi_{n\nu lm}(r_\infty)$  with the asymptotic boundary condition

$$\phi_{n\nu lm}(r) \xrightarrow{r \rightarrow \infty} k_{n_0\nu_0}^{-1/2} \hat{j}_l(k_{n_0\nu_0} r) \delta_{nn_0} \delta_{\nu\nu_0} \delta_{ll_0} \delta_{mm_0} + k_{n\nu}^{-1/2} \hat{n}_l(k_{n\nu} r) K_{n\nu lm, n_0\nu_0 l_0 m_0}, \quad (\text{SM23})$$

where  $\hat{j}_l(z)$  and  $\hat{n}_l(z)$  are the Riccati-Bessel functions, and  $K_{n\nu lm, n_0\nu_0 l_0 m_0}$  are elements of the  $K$  matrix, corresponding to the scattering from the incident channel  $(n_0\nu_0 l_0 m_0)$  to the outgoing one  $(n\nu lm)$ . Moreover,  $k_{n_0\nu_0}$  and  $k_{n\nu}$  are the relative momenta for the incident and outgoing channels, respectively. In numerical calculations, we introduce a truncation  $n_{\text{cut}}$  for the Floquet Hamiltonian such that  $|n| \leq n_{\text{cut}}$ . Practically, it is found that, for control parameters covered in this work, the scattering solutions converge when  $n_{\text{cut}} = 5$ .

To proceed further, we denote the  $K$  matrix as  $\mathbf{K}$ , from which one can obtain the scattering matrix  $\mathbf{S} = (1 + i\mathbf{K})(1 - i\mathbf{K})^{-1}$ . Now, the total elastic cross section for the incident channel  $(n_0\nu_0)$  is

$$\sigma_{n_0\nu_0}^{(\text{el})} = \frac{2\pi}{k_{n_0\nu_0}^2} \sum_{lml_0m_0} |\delta_{ll_0} \delta_{mm_0} - S_{n_0\nu_0 lm, n_0\nu_0 l_0 m_0}|^2, \quad (\text{SM24})$$

where  $S_{n_0\nu_0 lm, n_0\nu_0 l_0 m_0}$  are the elements of the scattering matrix.  $l$  and  $l_0$  are even (odd) for bosons (fermions). For elastic scattering, the outgoing channel of the molecules is the same as incident channel  $(n_0\nu_0)$  and the total kinetic energy of the molecules is thus conserved. Next, the total inelastic cross section can be calculated by subtracting the total elastic cross section from the total cross section, i.e.,

$$\sigma_{n_0\nu_0}^{(\text{inel})} = \frac{2\pi}{k_{n_0\nu_0}^2} \sum_{lml_0m_0} (\delta_{ll_0} \delta_{mm_0} - |S_{n_0\nu_0 lm, n_0\nu_0 l_0 m_0}|^2). \quad (\text{SM25})$$

It is instructive to distinguish, depending on whether the total energy of the colliding molecules is conserved, the degenerate and nondegenerate inelastic scatterings which are disguised in Eq. (SM25). Specifically, for degenerate

inelastic scatterings, the outgoing molecules remain in the same Floquet sector  $n_0$  but transit to the lower dressed-state channel  $\nu$  ( $> \nu_0$ ). Thus the total energy of the colliding molecules is conserved. While for nondegenerate inelastic scatterings, the outgoing molecules transit to a distinct Floquet sector  $n$  ( $\neq n_0$ ) by absorbing or emitting microwave photons and thus the total energy of the colliding molecules is not conserved. These the energy exchange processes mediated by the absorption and emission of dual microwaves lead to inelastic scattering and heating.

The experimentally more relevant quantities are the elastic and inelastic scattering rates, i.e.,  $\beta_{01}^{(\text{el})} = v_{01}\sigma_{01}^{(\text{el})}$  and  $\beta_{01}^{(\text{inel})} = v_{01}\sigma_{01}^{(\text{inel})}$ , where  $v_{01} = 2\hbar k_{01}/M$  is the relative velocity. In addition, the ratio of the elastic to inelastic scattering rates,  $\gamma = \beta_{01}^{(\text{el})}/\beta_{01}^{(\text{inel})}$ , is of particular importance for characterizing the efficiency of the evaporative cooling. Finally, from the  $K$  matrix, we may compute for small  $k_{01}$  the scattering length matrix according to  $\mathbf{a} = -\mathbf{K}/k_{01}$ , whose element  $a_{n\nu lm, n_0\nu_0 l_0 m_0}$  is the scattering length from the incident channel ( $n_0\nu_0 l_0 m_0$ ) to the outgoing channel ( $n\nu lm$ ). In particular, the  $s$ -wave scattering length for MSPMs is  $a_s = a_{0100,0100}$ .

To validate the effective potential, we also solve the Schrödinger equation

$$H_{\text{eff}}\psi(\mathbf{r}) = \frac{\hbar^2 k_{01}^2}{M}\psi(\mathbf{r}) \quad (\text{SM26})$$

using log-derivative propagator method. Here,  $k_{01}$  is the incident momentum, and the single-channel model for the relative motion of two MSPMs is then governed by the Hamiltonian

$$H_{\text{eff}} = \frac{\mathbf{p}^2}{M} + V_{\text{eff}}(\mathbf{r}). \quad (\text{SM27})$$

Making use of the partial-wave expansion,  $\psi(\mathbf{r}) = \sum_{lm} r^{-1} \phi_{lm}(r) Y_{lm}(\hat{\mathbf{r}})$ , the radial wave functions satisfy

$$-\frac{1}{M} \left[ \frac{d^2}{dr^2} - \frac{l(l+1)}{r^2} \right] \phi_{lm}(r) + \sum_{l'm'} [V_{\text{eff}}(r)]_{lm, l'm'} \phi_{l'm'}(r) = \frac{k_{01}^2}{M} \phi_{lm}(r), \quad (\text{SM28})$$

where the interaction matrix elements

$$[V_{\text{eff}}(r)]_{lm, l'm'} = \int d\hat{\mathbf{r}} Y_{lm}^*(\hat{\mathbf{r}}) V_{\text{eff}}(\mathbf{r}) Y_{l'm'}(\hat{\mathbf{r}}). \quad (\text{SM29})$$

In analogy to the multichannel case, we numerically solve Eqs. (SM28) and compute the low-energy scattering length  $a_{lm, l_0 m_0}$  for the scattering from incident channel ( $l_0 m_0$ ) to the outgoing one ( $lm$ ). Particularly, we focus on the  $s$ -wave scattering length  $a_s = a_{00,00}$ .

In Fig. SM2d, we compare the  $s$ -wave scattering lengths  $a_{0100,0100}$  and  $a_{00,00}$  obtained from the full-channel calculation and the effective potential (SM17) as a function of the elliptic angle  $\xi > 0$ . As  $\xi$  increases from zero, the positive  $C_{3,2}$  deepens the potential along the  $y$ -direction. When  $\xi$  reaches  $\xi_{\text{res}} = 9.2^\circ$ , the enhanced attractive interaction becomes strong enough to induce a shape resonance. Beyond this angle, a bound state emerges in the potential valley [see Fig. SM2b]. Notably, the two approaches yield quantitatively consistent results away from resonance. Even near the resonance, excellent agreement is maintained, with the resonance position differing by less than  $0.4^\circ$ . These results confirm the reliability of the effective potential  $V_{\text{eff}}(\mathbf{r})$  in capturing molecular collision dynamics under an elliptically polarized microwave field.

#### SM 4. SUPERFLUID FRACTIONS

In Fig. SM3, we show the superfluid fractions  $f_{\text{sf}}^{(x,y,z)}$  by changing the ellipticity and the trap frequency  $\omega_y$ .

Figure SM3(a) shows the superfluid fraction for a fixed trap frequency  $\omega_y = 2\pi \times 100\text{Hz}$ . Among the three directions, the superfluid fraction  $f_{\text{sf}}^{(x)}$  is dominant, reflecting higher stiffness corresponding to a larger critical rotational frequency along the  $x$  axis. The anisotropy of  $f_{\text{sf}}^{(x,y,z)}$  arises from the interplay between the trap geometry and DDI. For  $\xi = 3.9^\circ$  and  $4.0^\circ$ , the persistence of a dominant  $f_{s,x}$  implies that coherence is established within each droplet of the array. Meanwhile, the finite values of  $f_{\text{sf}}^{(y,z)}$  suggest phase coherence between distinct droplets, a hallmark of supersolidity. As  $\xi$  increases beyond  $4.2^\circ$ ,  $f_{\text{sf}}^{(y,z)}$  drop significantly, indicating the breakdown of long-range phase coherence between droplets in the array along the  $x$  direction. For even larger elliptic angles, such as  $\xi = 4.6^\circ$ , the strong long-range attraction along the  $y$  axis collapses the system into a single, high-density droplet. In this regime, the narrow size of the droplet suppresses the exchange of world lines in both the  $x$ - $z$  and  $x$ - $y$  planes, and inhibits phase coherence along

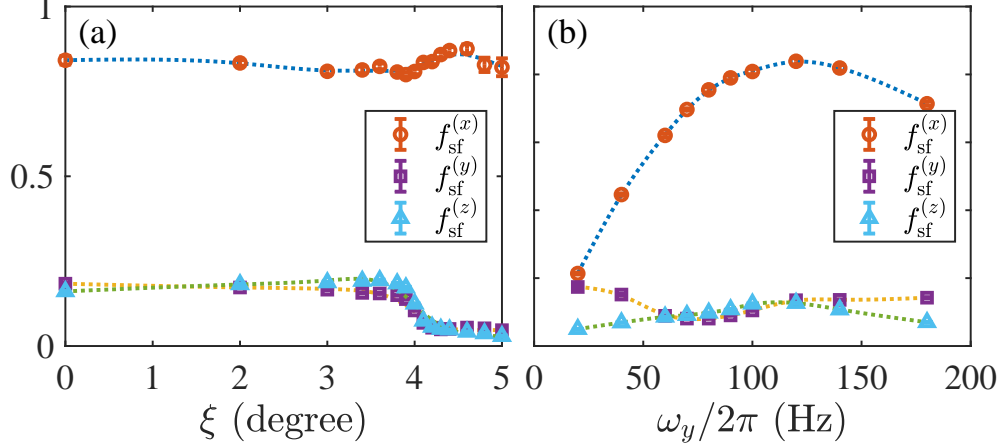


FIG. SM3. Superfluid fractions are averaged over 40-64 random seeds for a fixed trap frequency  $\omega_y = 2\pi \times 100\text{Hz}$  (a) and for a fixed ellipticity  $\xi = 4^\circ$  (b).

the  $x$ -direction, as coherence typically builds up over several  $r_0$  due to the strong shielding potential. As a result, both  $f_{\text{sf}}^{(y,z)}$  are reduced.

Figure SM3(b) shows the superfluid fraction for a fixed elliptic angle  $\xi = 4^\circ$ . For a small trap frequency  $\omega_y = 2\pi \times 20\text{Hz}$ , the superfluid fraction  $f_{\text{sf}}^{(x)}$  is much lower than that in Fig. SM3(a), as a result of a larger size in the  $y$ - $z$  plane [cf. Figs. 4(a1) in the main text] [S39]. As the trap is compressed (e.g.,  $\omega_y/(2\pi) = 60, 80, 100\text{Hz}$ ), the system crystallizes along the  $x$ -direction, forming a droplet array with lower density. The reduced size in the  $y$ -direction enhances superfluid fraction  $f_{\text{sf}}^{(x)}$ , while the nonvanishing components  $f_{\text{sf}}^{(y,z)}$  indicate coherence between different droplets and the emergence of a supersolid phase. This occurs because the droplets begin to merge, and the increased interparticle distance along the  $x$ -direction reduces the influence of short-range repulsion. With further increase in trap frequency beyond 120Hz, each droplet elongates along the  $x$ -direction. Eventually, the droplets merge together, forming a continuous gas extended along the  $x$ -direction. In this regime, most molecules are redistributed from the attractive ( $y$ -) direction to the repulsive ( $z$ - and  $x$ -) directions. The narrow size along the  $y$ -direction makes it difficult to exchange worldlines in the  $y$ - $z$  plane [S40], thereby reducing  $f_{\text{sf}}^{(x)}$ .